CrossMark

JFM PAPERS

Experimental study of the effects of droplet number density on turbulence-driven polydisperse droplet size growth

M. Shyam Kumar[1], Manikandan Mathur[1],† and S.R. Chakravarthy[1]

[1]Department of Aerospace Engineering, Indian Institute of Technology Madras, Chennai 600036, India

Interaction of polydisperse droplets in a turbulent air flow features prominently in a wide range of phenomena, such as warm rain initiation as an example. In the current study, we present an experimental investigation on the effects of initial droplet field characteristics on the maximum droplet size growth. By performing experiments in a vertically oriented air flow facility, the air flow turbulence was able to be controlled through the mean flow velocity and an active turbulence generator. The initial droplet field characteristics (droplet diameter range of 0–120 μm) were varied using spray nozzles of different flow numbers. Based on quantitative measurements of the droplet size distribution at various spatial locations using phase Doppler interferometry (PDI), we estimated the droplet size growth rate R as a function of turbulence intensity I, initial droplet number density ρ_N and initial mean droplet size $\bar{D}$. For each (ρ_N, $\bar{D}$), we observed the occurrence of an optimum turbulence intensity I^*, with the corresponding maximum droplet size growth rate being R^*. Two different trends were observed. When ρ_N and $\bar{D}$ were simultaneously increased and decreased, respectively, their competing influences resulted in small variations in R^*. In contrast, when $\bar{D}$ was held constant with a corresponding Stokes number St smaller than unity, there existed a threshold ρ_N above which R^* increased rapidly with ρ_N. These trends were then understood through long-distance microscopy (LDM) measurements. Beyond the aforementioned threshold ρ_N, the fraction of uncorrelated small-sized ($St < 1$) droplet pairs was found to rapidly increase with ρ_N. Further detailed analysis of droplet tracking in the LDM images identified that the velocity fluctuations in the small-sized droplet pairs being induced by close encounters with inertial droplets was the underlying mechanism for the rapid increase of R^* with ρ_N. This mechanism potentially explains how droplet collisions can be enhanced in small droplets if the droplet field is sufficiently polydisperse.

Key words: multiphase flow, breakup/coalescence, particle/fluid flow

† Email address for correspondence: manims@ae.iitm.ac.in

1. Introduction

Particle dynamics in a turbulent flow are an important consideration in several applications, which range from small-scale phenomena like transport of blood corpuscles in the human body (Dooley & Quinlan 2009) to large-scale astrophysical flows (Bracco *et al.* 1999). Sediment transport in rivers and oceans, pollutant transport in the atmosphere, volcanic ash eruptions and fluidised bed reactors are some of the more commonplace applications. The dynamics associated with particle interactions in a turbulent flow becomes richer when the particles are fluid too, as in air bubbles in a turbulent liquid flow (Balachandar & Eaton 2010) or liquid droplets in a turbulent air flow (Grabowski & Wang 2013). The latter scenario, which is of great interest in propulsion systems (Reveillon & Vervisch 2005) and warm rain initiation (Wilkinson, Mehlig & Bezuglyy 2006), is the topic of the current study. Specifically, we investigate droplet size growth arising from coalescence in a background turbulent air flow, a mechanism thought to be of significance in warm rain formation (Falkovich, Fouxon & Stepanov 2002).

Droplet size growth arising from air turbulence depends directly on droplet collision rates, although collisions do not necessarily result in coalescence. An estimation of droplet collision rates therefore represents an important first step towards an understanding of trends in the evolution of droplet size in turbulent flows. The parameters that influence droplet collision rates include both turbulent flow features, such as its length scales and intensity (Vaillancourt & Yau 2000), and droplet features, such as its size distribution, volume fraction and the liquid density (Freud & Rosenfeld 2012). Owing to the strong coupling between these various parameters, accounting for all of their effects simultaneously on droplet collision rates is challenging. For similar-sized droplets, whose size is much smaller than the Kolmogorov length scale of the turbulent flow, their collision rates depend primarily on the droplet size, the droplet number density, the turbulence dissipation rate and the air kinematic viscosity (Saffman & Turner 1956). For particles much larger than the Kolmogorov length scale, Abrahamson (1975) used kinetic theory to estimate their collision rates. The collision rates in intermediate particles, however, are poorly captured by both the small- and large-droplet theories. By performing direct numerical simulations for intermediate-sized particles in the dilute limit, Sundaram & Collins (1997) highlighted two important effects, namely preferential concentration (i.e. spatial inhomogeneity in local number density) and particle decorrelation (increased relative velocity between droplets), which enhance collision rates. Several studies have since focused on various mechanisms that affect the preferential concentration and particle decorrelation effects.

In regards to preferential concentration, two primary mechanisms have been discussed in the literature. Particles whose density is much larger than air density and of Stokes number $St \sim 1$ tend to get centrifuged out of turbulent eddies and accumulate in low-vorticity regions (Maxey 1987; Squires & Eaton 1991; Eaton & Fessler 1994; Jacobs *et al.* 2016). This clustering can in turn locally increase the droplet number density, and hence increase the droplet collision rates in turbulent flows with a small mean flow (Sundaram & Collins 1997). The centrifugal mechanism, however, is relatively less effective at St far from unity. In contrast to clustering arising from a centrifugal mechanism, where the small scales significantly influence clustering, large inertial particles usually undergo multi-scale clustering (Coleman & Vassilicos 2009). The physical mechanism attributed to a preferential concentration for $St > 1$ is the sweep-stick mechanism (Goto & Vassilicos 2008). In the sweep-stick mechanism, inertial particles have been shown to accumulate in zero-acceleration regions, with the resulting cluster convecting with the carrier fluid (Goto & Vassilicos 2008; Monchaux, Bourgoin & Cartellier 2012). The effect of this sweep-stick

clustering mechanism on droplet collision rates is not well understood. Furthermore, large-scale flow anisotropy can also enhance particle collisions by introducing anisotropy in the geometric configurations of small-scale clustering even if the turbulence is isotropic at small scales (Gualtieri *et al.* 2012).

In regards to particle decorrelation, various mechanisms, namely caustics (Wilkinson *et al.* 2006), sling effect (Falkovich *et al.* 2002) and differential settling velocity (Good *et al.* 2014; Jacobs *et al.* 2016), have been discussed. Caustics (Bec *et al.* 2010) and the sling effect (Voßkuhle *et al.* 2014) both lead to enhanced droplet collisions beyond a threshold turbulence intensity by inducing a very high relative velocity even at small separation distances. While the underlying mechanism in caustics is the multi-valued velocity field in phase space (Wilkinson *et al.* 2006), the sling effect concerns particles being 'slung' by vortices (Falkovich & Pumir 2007). However, droplet collisions induced by differential settling, which results from particle inertia, are relatively weak (Voßkuhle *et al.* 2014).

While several studies have focused on monodisperse droplet fields, real-world droplet fields, such as clouds, are polydisperse, i.e. they comprise a finite range of droplet sizes. Indeed, droplet collisions followed by coalescence may itself be responsible for introducing polydispersity in a monodisperse droplet field. The dynamics across different droplet sizes in a polydisperse droplet field may introduce non-trivial effects that are absent in monodisperse droplets. For polydisperse droplet fields, studies on droplet collisions have focused either on preferential concentration (Reade & Collins 2000; Aliseda *et al.* 2002) or particle decorrelation (James & Ray 2017). Preferential concentration and particle decorrelation are, however, physically coupled (Bec *et al.* 2005). A recent experimental study (Kumar, Chakravarthy & Mathur 2019) showed that for a given polydisperse droplet field in which preferential concentration and particle decorrelation simultaneously occur in a turbulent air flow with a strong mean component, there exists an optimum turbulence intensity for which droplet size growth is maximised. They report that the onset of clustering suppresses the intuitive effect of an increase in droplet collision rate with air turbulence intensity, which results in the existence of an optimum air turbulence intensity that maximises the average droplet size growth rate arising from droplet coalescence. The study by Kumar *et al.* (2019) was restricted to a fixed initial droplet field, and hence did not investigate the effects of the initial droplet characteristics.

In this paper, we report on the effects of mean droplet size and number density on the droplet size growth rate in a strongly polydisperse droplet field in a background turbulent air flow. The rest of the paper is organised as follows. Section 2 describes the set-up, which includes the various measurement techniques used in this study, and lists the various experimental parameters and their values. The experimental results, along with a detailed interpretation using various post-processing tools, are presented in § 3. Our results are summarised in § 4, followed by a brief discussion of the relevance of our results to warm rain initiation.

2. Methodology

The experimental set-up consisted of a vertically oriented air flow facility, at the top of which air flow at a desired mass flow rate entered through an inlet manifold. The air flow then passed through honeycomb structures (having holes with a diameter of 5 mm) and a converging duct of a square cross-section, as shown in figure 1(*a*). Within the constant area duct placed downstream of the converging duct, an ATG (Mulla, Sampath & Chakravarthy 2019) was placed that imparted turbulence on the incoming flow. Polydisperse water droplets with diameters in the range of 0–120 μm were introduced into the turbulent
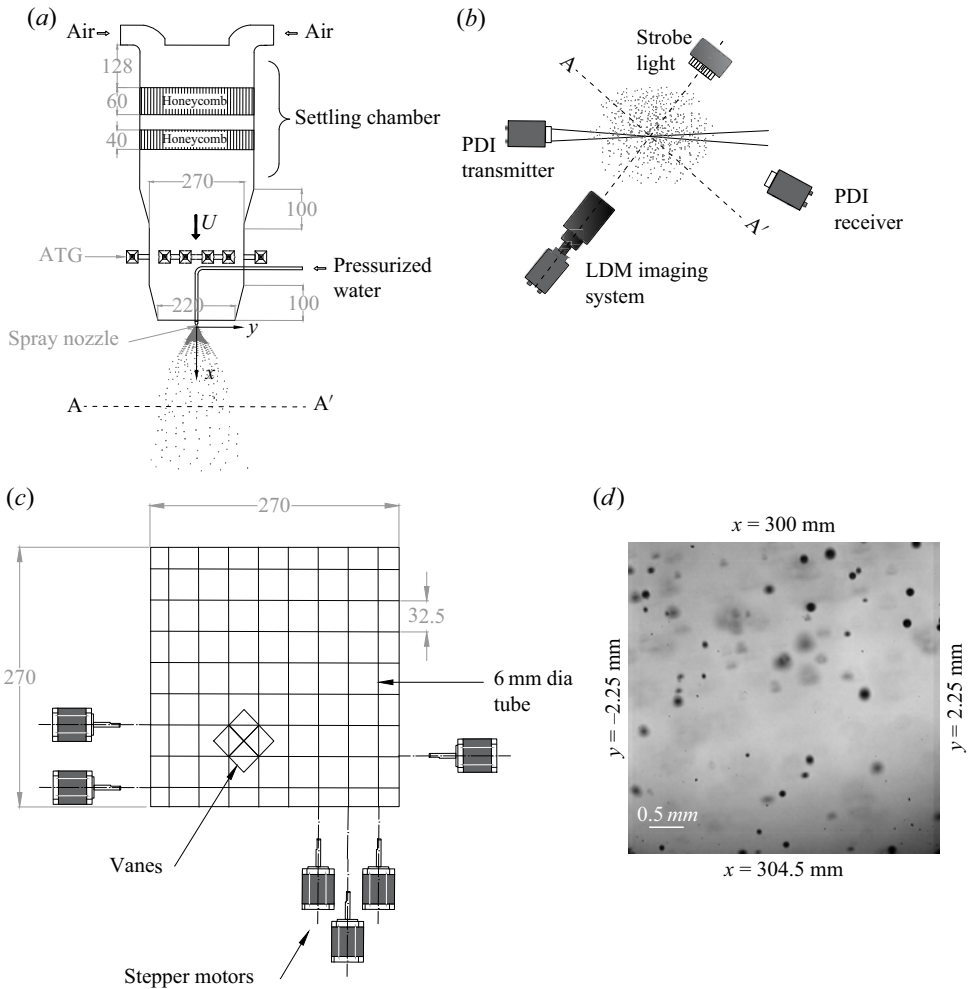
Figure 1. (a) Schematic of the experimental set-up, with all dimensions in mm. The axial and transverse directions are specified by the x- and y-axes, respectively, with the origin placed at the spray nozzle exit. (b) Top view of the AA′ plane indicated in (a), along with the optical arrangements for the phase Doppler interferometry (PDI) and long-distance microscopy (LDM) measurements. (c) Schematic representation of the active turbulence generator (ATG), with 8 horizontal and 8 vertical rods arranged in a 270 mm × 270 mm square region. (d) A representative image obtained using LDM over a 4.5 mm × 4.5 mm window centred around $(x, y) = (302.25, 0)$ mm.

air flow through a spray nozzle placed at the air flow exit (figure 1a). We defined a xy coordinate system such that x is the axial distance from the spray nozzle exit and y is the transverse coordinate measured from the central axis.

The ATG comprised a series of rotating vanes arranged on a 270 mm × 270 mm square cross-section, driven by 24 independently controlled stepper motors. A schematic of the ATG is shown in figure 1(c). A grid spacing (M) of 32.5 mm was used to fit eight horizontal and vertical shafts arranged in the 270 mm × 270 mm ($8M \times 8M$) square box (figure 1c). To reduce inertia, instead of rods, tubes with an inner diameter of 6 mm and a wall thickness of 1 mm were used. The horizontal shafts and vertical shafts were placed at different planes which were separated by 11 mm. Aluminium vanes, with a chord length

of 31.6 mm and thickness of 0.5 mm, were mounted on the tube alternatively on each side of the rod. Each rod was connected to a stepper motor through deep groove ball bearings. The angular velocity was modelled as a random variable and the rotation profile of the vanes controlled the turbulence intensity imparted to the air flow. Another converging duct, placed downstream of the ATG, improved the isotropy of turbulence before the air flow exited into the open surroundings.

Two different measurement techniques were employed to characterize the droplet field in a region that was sufficiently far from the spray nozzle exit. Phase Doppler interferometry (Bachalo 1997) was used to measure the distributions of droplet diameter and velocity at different axial and transverse locations. In addition, the PDI data were also used to estimate the droplet number density, following the algorithm described in Qiu & Sommerfeld (1992) and Borée, Ishima & Flour (2001). Long-distance microscopy was used to visualize individual droplet events and subsequently compute statistical measures of these events. The *Artium*-made PDI set-up consists of a 500 mm focal length transmitter and receiver, which measures droplet sizes in the range of 0.3–8000 µm with an accuracy of ±0.5 µm. The LDM set-up consisted of a strobe light source that was placed approximately 1 m from the central axis, and a high-speed camera (FASTCAM series from Photron with a maximum resolution of 1024×1024 at 5400 Hz and a minimum of 128×16 at 500 000 Hz) fitted with a microscope (QM-100 model from Questar with manual focusing) that captured images at 10 000 Hz with 768 pixels $\times$ 768 pixels on the camera representing the 4.5 mm $\times$ 4.5 mm field of view with a 3.5 mm depth of field. Figure 1(*b*) shows the optical arrangements for both PDI and LDM. A sample LDM image is shown in figure 1(*d*), which typically captured a couple of tens of droplets in a single frame. The frame resolution was such that a 60 µm droplet occupied approximately 10 pixels in each direction. We also performed three-dimensional laser Doppler velocimetry (LDV) measurements without the spray, with olive oil droplets of 1 µm acting as seeding particles, to quantify the turbulent intensity at various experimental settings.

The PDI, LDM and LDV measurements were performed in a region that was sufficiently downstream of the spray nozzle such that transverse variations of droplet characteristics were negligible, and thus indicated a good mixing of the droplet field and the background turbulent air flow. Accordingly, the measurement region was identified as the rectangular domain specified by $-20 \leq y \leq 20$ and $200 \leq x \leq 400$ mm. Experimental measurements showing transverse uniformity in this region have been reported by Kumar *et al.* (2019). Specifically, PDI and LDV measurements were performed at various transverse and axial locations within the measurement region, while LDM was focused on a smaller subset region given by $-2.25 \leq y \leq 2.25$ and $300 \leq x \leq 304.5$ mm (see figure 1*d*). Various flow and droplet characteristics were estimated from the LDV and PDI measurements, based on the expressions given in Appendix A.

For a given spray nozzle operating at a fixed injection pressure, experiments were run at different air flow turbulence intensities (*I*). *I* was varied by changing two different parameters: (i) the uniform air flow speed *U* just upstream of the ATG (see figure 1*a*) and (ii) the maximum rotational speed ω of the ATG vanes. For a given *U* and ω, the variation of *I* in the transverse and axial directions within the measurement region was weak. Table 1 shows the different values of *I*, estimated as the spatial average of the LDV-based turbulence intensity within the measurement region, achieved in our experiments through appropriate changes in *U* and ω. As shown in table 1, *I* was varied between 10.5 % and 16.3 %, while the anisotropy across all the experiments remained reasonably weak. In addition, several derived quantities were estimated from the LDV data, as detailed

U (m s^{-1})	ω (rpm)	I (%)	α	η (μm)	L (mm)	Re_λ
0.82	0	10.5	$1.07 \pm .06$	232	27	64
0.77	300	10.7	$1.11 \pm .03$	222	28	71
0.77	750	11.4	$1.12 \pm .04$	210	28	72
0.88	750	11.5	$1.11 \pm .04$	201	29	74
1.30	0	12.2	$1.14 \pm .03$	168	29	78
1.30	150	12.9	$1.12 \pm .03$	150	31	81
1.30	750	14.2	$1.14 \pm .03$	160	31	88
1.73	0	15.2	$1.14 \pm .02$	148	32	93
1.73	1125	15.8	$1.17 \pm .04$	132	33	92
1.81	750	16.3	$1.17 \pm .06$	126	34	101

Table 1. Turbulence intensity (I), anisotropy (α), Kolmogorov length scale (η), integral length scale (L) and Reynolds number based on the Taylor microscale (Re_λ) achieved by varying the mean axial air velocity U just upstream of the ATG and the maximum rotational speed ω of the ATG vanes.

in Appendix A. The integral length scale L remained nearly constant (approximately 30 mm) across all the flow conditions with different turbulent intensities. Finally, the Reynolds number based on the Taylor microscale Re_λ, shown in the last column of table 1, monotonically increased with I.

The droplet characteristics that were present upstream of the measurement region were varied by changing either the spray nozzle (in other words, using a pressure swirl atomizer) or the operating injection pressure. Spray nozzles are typically characterized by the flow number, which is defined as

$$Flow\ no. = \dot{m}/\sqrt{(\Delta P)(\rho_f)}, \qquad (2.1)$$

where $\dot{m}$ is the mass flow rate of the fluid (water) through the spray nozzle orifice, ΔP is the pressure drop (difference between the injection pressure and the atmospheric pressure) and ρ_f is the fluid density. Eleven different cases were realized, each corresponding to a unique flow no. of the spray nozzle (table 2). For a given spray nozzle, a large increase in injection pressure is needed for a small increase in $\dot{m}$. In cases 1–11, the mass flow rate $\dot{m}$ increased monotonically, but the flow no. did not. For the droplet field characteristics, specifically the droplet number density and the mean droplet size, $\dot{m}$ plays a more critical role. Figure 2(a) shows the global droplet size distribution, which was estimated using PDI measurements from multiple y locations at $x = 100$ mm, for cases 1, 5 and 10.

As the flow number was increased, the droplet size distribution shifted towards smaller diameters, while the width of the main peak also decreased. In physical terms, the mean diameter ($\bar{D}$) and the polydispersity both decreased in going from cases 1 to 5 to 10. The polydispersity was quantified using the parameter SMD/$\bar{D}$ (see Appendix A for definitions of $\bar{D}$ and the Sauter mean diameter SMD), which would be equal to and larger than unity for monodisperse and polydisperse droplet fields, respectively. Larger values of SMD/$\bar{D}$ indicated a larger polydispersity. Indeed, plots of the mean diameter $\bar{D}$ (figure 2b) and a measure of the polydispersity SMD/$\bar{D}$ (figure 2c) both showed a monotonic decrease with case no. Along with $\bar{D}$ and SMD/$\bar{D}$, the droplet number density ρ_N also changed across cases, which showed a monotonic increase with case no. (figure 2d). For each of the 11

| Case no. | $\dot{m}$ | Injection pressure | Flow no. |
(−)	($\times 10^{-3}$ kg s^{-1})	(bar)	($\times 10^{-8}$ m^2)
1	1.1	4	5.26
2	2.1	4	10.5
3	2.6	4	13.2
4	3.2	4	15.8
5	3.4	6	14
6	3.5	8	12.3
7	3.7	4	18.4
8	3.9	6	16.1
9	4.2	8	14.9
10	4.5	4	22.4
11	4.7	6	19.3

Table 2. Case no. and corresponding flow no. achieved by varying the injection pressure for different spray nozzles.
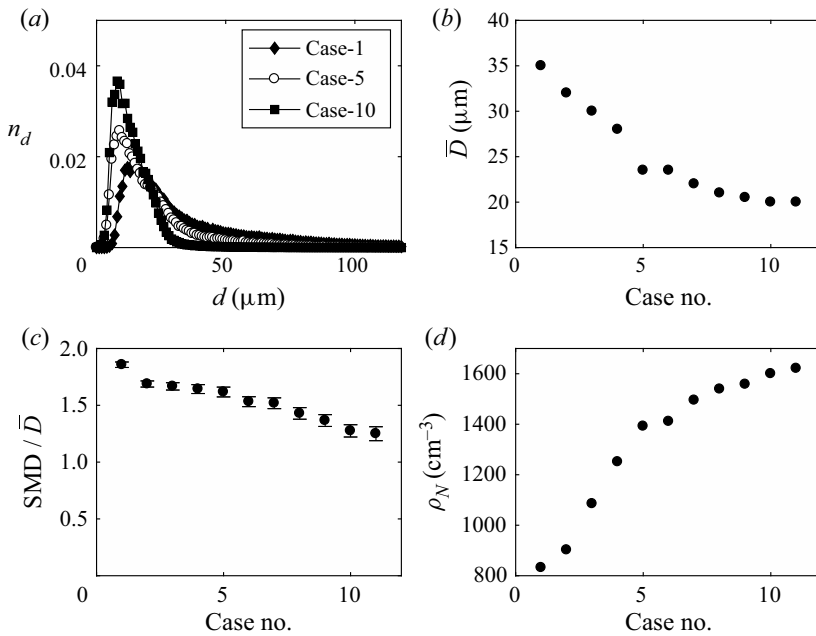
Figure 2. Droplet field characterization at $x = 100$ mm for various spray nozzle cases. (*a*) Global droplet size distribution (A1) for three different spray nozzle cases. Variation of (*b*) the mean droplet diameter $\bar{D}$, (*c*) the polydispersity parameter SMD/$\bar{D}$ and (*d*) the droplet number density ρ_N for the eleven different spray nozzle cases listed in table 2.

spray nozzle cases, we ran experiments at the ten different turbulent intensities shown in table 1.

In regards to polydispersity, while SMD/$\bar{D}$ changed across the cases (figure 2*c*), every spray nozzle case still contained a wide range of droplet sizes. Therefore, while polydispersity plays an important dynamic role in our study, we neglected the effect of changing SMD/$\bar{D}$ with case no. The mean diameter $\bar{D}$ changed appreciably across cases 1 to 7, while $\bar{D}$ changed minimally (by a value that was close to the PDI measurement
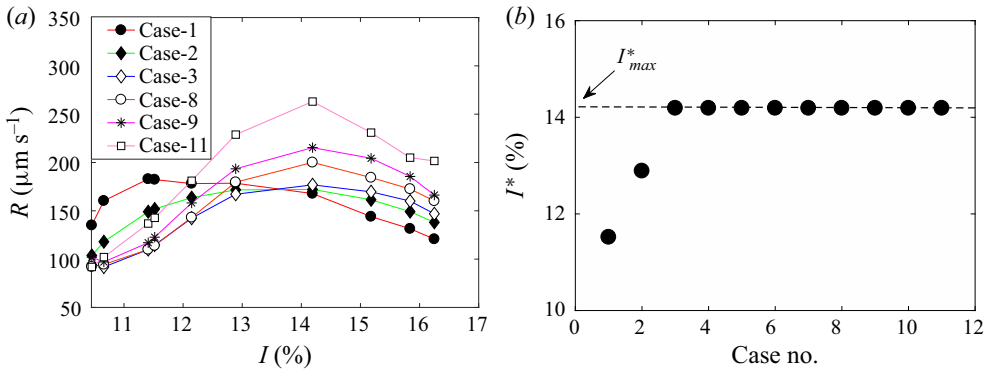
Figure 3. (*a*) Non-monotonic variation of droplet size growth rate *R* with turbulence intensity *I* for the spray nozzle cases indicated in the legend. (*b*) Variation of the optimum turbulence intensity I^* (at which maximum droplet size growth rate R^* occurs) with different spray nozzle case numbers.

error of 0.5 μm) across the last four cases (figure 2*b*). In contrast, the change in ρ_N was significant across all cases (figure 2*d*), which suggested that ρ_N may play a more important role than $\bar{D}$ in determining the changes in dynamics across the last few cases. Furthermore, we defined the Stokes number $St = (\rho_d/\rho_a)(d_p/\eta)^2/18$, where ρ_d and ρ_a are the liquid and air densities and η is the Kolmogorov length scale. Across the eleven cases listed in table 2, *St* varied from 1.6 to 0.9 at the mean droplet diameter $d_p = \bar{D}$ and $I = 14.2\%$. The Kolmogorov length scale η was estimated based on LDV measurements in the flow without the droplet field; it would, however, become modified in the presence of the droplet field, an effect that we do not take into account in our estimation of the Stokes numbers.

3. Results and discussion

As mentioned in §2, for each spray nozzle case, the droplet size growth in the measurement region was quantified using PDI for ten different values of *I*. In each experiment, the droplet size growth rate was estimated as $R = \mathrm{d}D_m/\mathrm{d}t_r$, where $D_m(x)$ is the axial variation of the mean droplet diameter, as has also been reported in Kumar *et al.* (2019). Here, the droplet residence time t_r between two axial locations x_1 and x_2 was estimated as $t_r = 2(x_2 - x_1)/[U_m(x_1) + U_m(x_2)]$, where $U_m(x)$ is the mean droplet axial velocity at the axial location *x*. Specifically, *R* was estimated by plotting D_m as a function of t_r based on measurements at five different axial locations in $x \in [200, 400]$ mm, and then calculating the slope of the best-fit straight line. Across all our experiments, the coefficient of determination of the straight line fits to D_m versus t_r was at least 0.93. Figure 3(*a*) shows the variation of *R* with *I* for six different spray nozzle cases. For each case, there existed an optimal $I = I^*$ for which *R* attained a maximum. The maximum droplet size growth rate R^* was observed to be somewhere between 1.4 to 2.9 times the smallest observed *R*, with the specific value depending on the case no. Plotting I^* with case no. showed that, barring cases 1 and 2, I^* was constant at a value of $I^*_{max} = 14.2\%$ (figure 3*b*). Motivated by the conclusions of Kumar *et al.* (2019) for a single spray nozzle (case 1), we verified that droplet clustering (quantified using the pair correlation function, Larsen, Kostinski & Tokay 2005) set in at the same turbulence intensity of $I = 14.2\%$ for all spray nozzle cases from 3 to 11. Plots of the pair correlation function from two different cases, which indicated the occurrence of clustering for $I > I^*$, are shown in Appendix B.
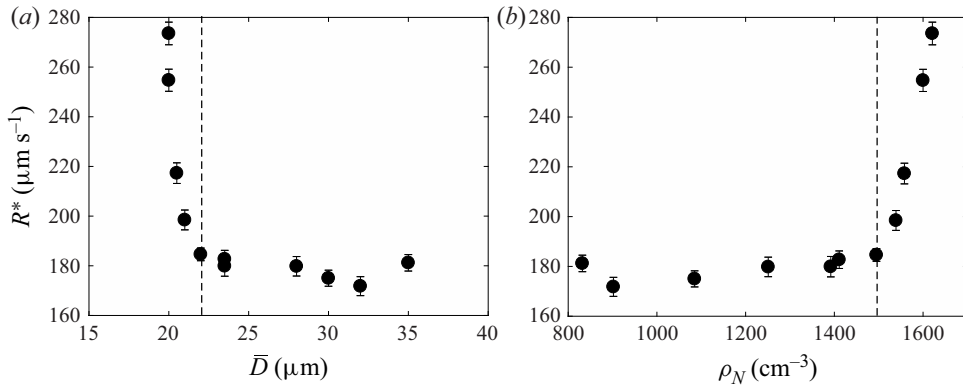
917 A12-8

Figure 4. Variation of maximum droplet size growth rate R^* with (*a*) mean droplet size $\bar{D}$ and (*b*) number density ρ_N for all the spray nozzle cases, as listed in table 2. The vertical dashed lines separate the regions of slow and rapid variation of R^*.

Figure 4 shows the variation of the maximum droplet size growth rate R^*, i.e. the measured R at $I = I^*$, with case no. Instead of plotting the case no. on the x−axis, we plotted the physical parameters $\bar{D}$ (figure 4*a*) and ρ_N (figure 4*b*), whose variation with case no. are presented in figure 2. Interestingly, an increase (decrease) in $\rho_N(\bar{D})$ did not significantly influence R^* up to some threshold values of ρ_N and $\bar{D}$, beyond which a sudden increase in R^* was observed. For $\bar{D} \geq 28$ μm, i.e. cases 1 to 4, the variation of R^* was weak with its value hovering at approximately 180 μm s^{-1}. With respect to ρ_N, R^* was relatively invariant for $\rho_N \leq 1250$ cm^{-3}. For cases 5–7, $\bar{D}$ was within the range of 23–22 μm, while ρ_N changed by approximately 100 cm^{-3}. Despite the appreciable change in ρ_N while $\bar{D}$ remained more or less constant, R^* still remained at approximately 180 μm s^{-1} for cases 5–7. For cases 7–11, however, we observed a rapid variation of R^*, with its value growing by a factor of 1.5 from case 7 to case 11. It is noteworthy that ρ_N changed by 126 cm^{-3} from case 7 to case 11, whereas $\bar{D}$ changed only by approximately 1 μm. In physical terms, as we go from case 7 to case 11, we are adding a progressively larger number of similar-sized small droplets within a given volume. In summary, figure 4 shows that there exists a threshold $\rho_N \approx 1500$ cm^{-3} above which the droplet size growth rate increases rapidly with ρ_N, while $\bar{D}$ remains relatively small at approximately 21 μm, which corresponds to $St \approx 0.9$ at $I = I^*$.

To gain a physical understanding of the trends observed in figure 4, it is relevant to provide a discussion in terms of the droplet collision rates in the different experiments. First, the collision rate of droplets in a turbulent flow increases with number density as the probability of finding nearby droplets increases (Monchaux, Bourgoin & Cartellier 2010; Sumbekova *et al.* 2017). However, a decrease in the mean droplet size of a polydisperse field, and hence the number of relatively large inertial droplets, reduces the collision rates associated with caustics (Wilkinson *et al.* 2006) or the sling effect (Falkovich *et al.* 2002). The aforementioned physical mechanisms, while being relevant, do not necessarily explain the main observation that R^* increases rapidly with ρ_N above a threshold ρ_N.

To delve further, we used LDM (see §2 for a description) to identify all droplet pairs within a small region (4.5 mm × 4.5 mm) and quantitatively characterized their collision likelihood in a statistical manner. Specifically, LDM images, such as those
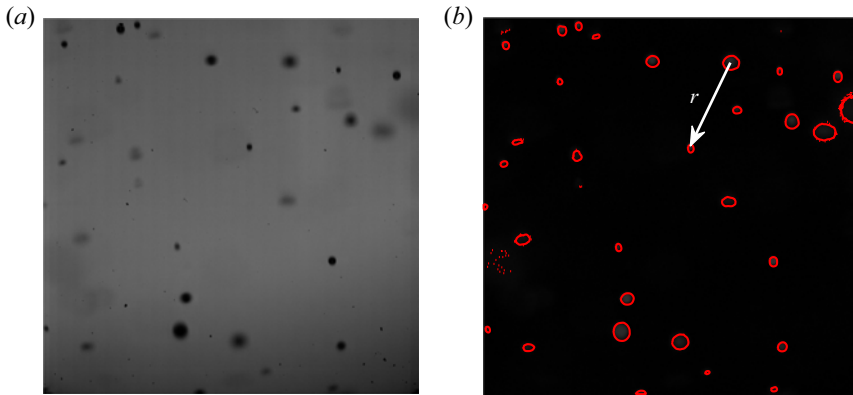
Figure 5. (*a*) A representative image of the droplet field obtained using LDM. (*b*) Post-processed image obtained after performing droplet boundary detection using the MATLAB image processing tool-box. *r* denotes the separation distance between two droplets.
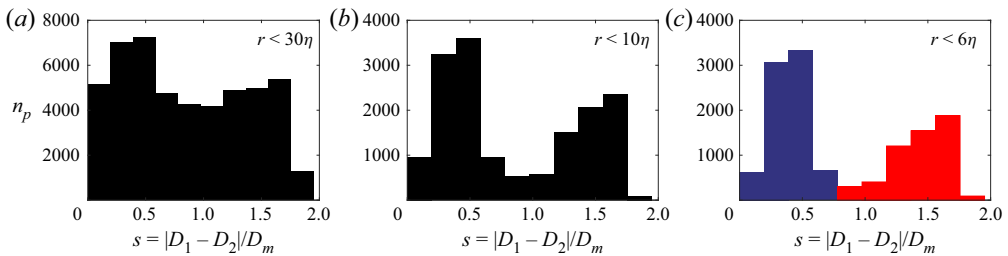

Figure 6. Droplet pair distribution for a separation distance of (*a*) $r < 30\eta$, (*b*) $r < 10\eta$ and (*c*) $r < 6\eta$ in the case-3 experiment. In (*c*), blue and red colours denote continuous and caustic pairs, respectively.

shown in figures 1 and 5(*a*), were first analysed (see Appendix C for details of the analysis) to identify all droplet boundaries in a given snapshot (figure 5*b*). After the droplet identification on 30 000 different snapshots, all droplet pairs were characterized in terms of the relative size difference $s = |D_1 - D_2|/D_m$ (D_1 and D_2 are the diameter of the droplets in a pair and $D_m = (D_1 + D_2)/2$) within the pair and the maximum separation distance r between the droplets within the region of interest. Histograms of n_p (number of droplet pairs in a given range of s from 30 000 snapshots) plotted against various bins in s were then calculated for different ranges of r.

Figure 6 shows the distribution of $s = |D_1 - D_2|/D_m$ for three different ranges of r in the $I = I^*$ experiment for the spray nozzle case 3 ($\rho_N = 1085 \text{ cm}^{-3}$, $\bar{D} = 30 \text{ μm}$). For $r < 30\eta$, which accounts for almost all the droplet pairs present over the region of $-2.25 \leq y \leq 2.25$ and $300 \leq x \leq 304.5$ mm, droplet pairs with any value of $s \in (0, 2)$ were observed (figure 6*a*). For $r < 10\eta$, however, we observed a preference for small ($0.2 \leq s \leq 0.6$) and large ($1.2 \leq s \leq 1.8$) values of s, as indicated by the two broad peaks in figure 6(*b*). A similar distribution was observed in figure 6(*c*), which is plotted for $r < 6\eta$. In physical terms, for sufficiently small separation distances r (which is a pre-requisite for droplet collisions), there mainly exists two types of droplet pairs: one where the two droplets are of comparable sizes (small s) and the other where the two droplet sizes are disparate (large s). For example, if one of the droplets has a diameter of 20 μm, the other would have a diameter of 27 μm if $s = 0.3$, and a diameter of 140 μm if $s = 1.5$.
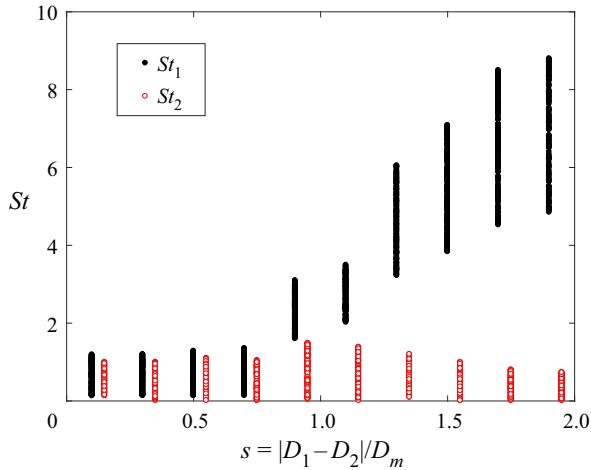
917 A12-10

Figure 7. Distribution of Stokes number St of the two droplets ($St_1 > St_2$) in each pair that satisfies $r < 10\eta$ in the case-3 experiment (corresponding number distribution shown in figure 6b).

To further investigate the droplet sizes in droplet pairs with small and large s, we re-plotted figure 6(b) with the Stokes number associated with each droplet being shown on the y-axis (figure 7). For each droplet pair within a given interval in s, the Stokes numbers associated with the larger (St_1) and smaller (St_2) droplet were calculated. St_1 and St_2 associated with all the droplet pairs within the given interval of s were then plotted in black and red, respectively, as shown in figure 7. Interestingly, droplet pairs with s in the range $0.2 \leq s \leq 0.8$ had comparable values for St_1 and St_2, which indicated small, similar-sized droplets. In contrast, for $s > 0.8$, the pairs contained one small ($St_2 < 1$) and one large ($St_1 > 1$) droplet. Following Wilkinson *et al.* (2006) and Pan & Padoan (2013) and using the results in figure 7, we denoted droplet pairs with small and large s as continuous pairs and caustic pairs, respectively. In general, while the droplet relative velocity decreases linearly with droplet separation distance for continuous pairs (Pan & Padoan 2013), the droplet relative velocity can be large even at small separation distances for caustic pairs (Wilkinson *et al.* 2006). The continuous ($0 \leq s \leq 0.8$) and caustic ($s > 0.8$) droplet pairs are indicated in blue and red, respectively, in figure 6(c).

We proceed to present sample continuous and caustic droplet pairs in LDM images from the same experiment as in figure 6, i.e. case 3. The white dashed box in figure 8(a) encompasses a droplet pair whose value of s is 0.22, thus representing a continuous pair. Interestingly, after 1.4 ms, the separation distance within the droplet pair had hardly changed (figure 8b), thus indicating that the two droplets had well-correlated velocities. Well-correlated velocities within droplet pairs arising from similar settling velocities have previously been reported in turbulent flows (Wang *et al.* 2006). The droplets within such correlated continuous pairs are unlikely to collide, and hence do not contribute to the overall droplet size growth. In contrast, the continuous droplet pair ($s = 0.18$) highlighted within the white dashed box in figure 8(c,d) showed a decreasing separation distance with time, and hence represents a likely candidate for collision. Similarly, we also observed continuous droplet pairs for which the separation distance increased with time. We termed such droplet pairs with decreasing or increasing separation distance, i.e. uncorrelated velocities for the droplets, as uncorrelated continuous pairs. In summary, among all the
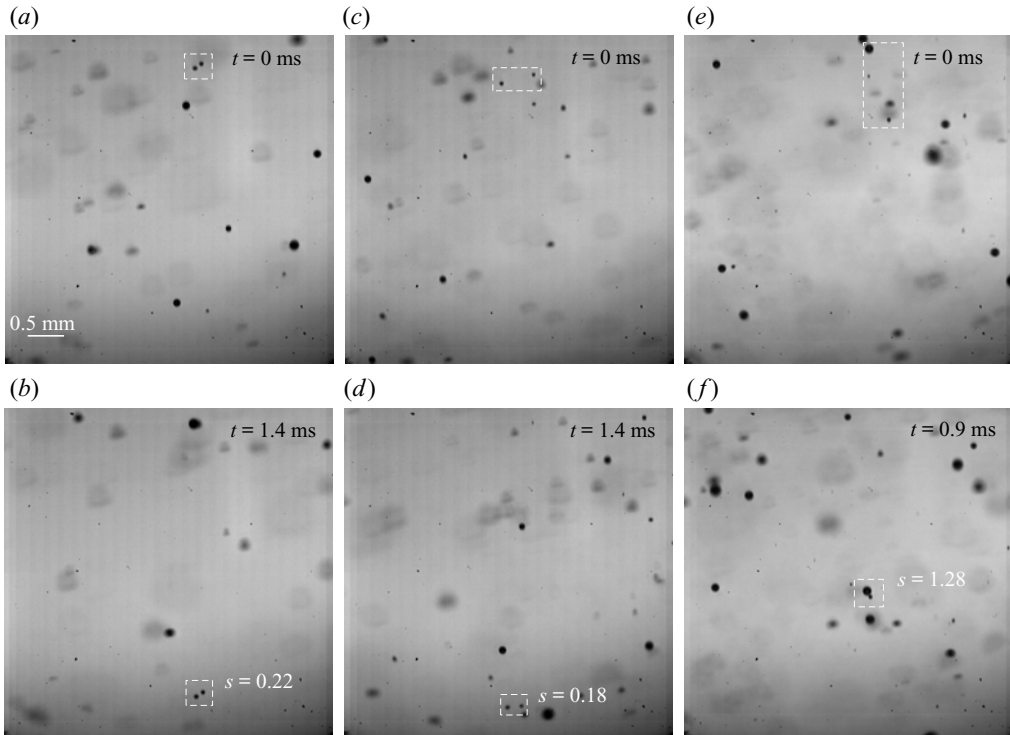
Figure 8. Representative LDM images showing (*a*,*b*) a correlated continuous pair, (*c*,*d*) a uncorrelated continuous pair and (*e*,*f*) a caustic pair, as highlighted by the white dashed boundaries in the respective images. The times corresponding to the images in the bottom row relative to those in the top row are indicated at the right top of the images. All the images were obtained in the case-3 experiment.

continuous pairs, some (uncorrelated) are likely to collide while the others (correlated) do not seem to contribute to collisions within reasonable times.

Unlike continuous droplet pairs, caustic droplet pairs have a larger relative velocity between the droplets. LDM images of one such caustic pair (with $s = 1.28$) are shown in figure 8(*e*,*f*), where a rapid decrease in the separation distance with time was observed. The relevance of caustic droplet pairs in enhancing collision rates in turbulent flows has previously been discussed (Wang *et al.* 2006; Wilkinson *et al.* 2006). In our study, however, the overall collision rates contained contributions from both caustic and uncorrelated continuous droplet pairs. We therefore proceeded to quantify the fraction of colliding pairs among both caustic and continuous pairs, which was achieved by specifying a threshold (corresponding to a change of at least a 20 % in the separation distance) on the ratio between the initial and final separation distances within the field of view in the LDM images. In terms of the radial relative velocity, this threshold corresponds to approximately $0.1 \, \mathrm{m \, s^{-1}}$ (see Appendix D for more details on radial relative velocity within droplet pairs). While a decreasing distance between droplets cannot be taken as evidence for collision, the probability distribution functions (PDFs) of the relative velocity and the range of s in various parts of the PDFs (Appendix D) certainly indicate a higher likelihood of collisions in small droplet pairs, which in turn is consistent with the observed trend in droplet size growth rates.
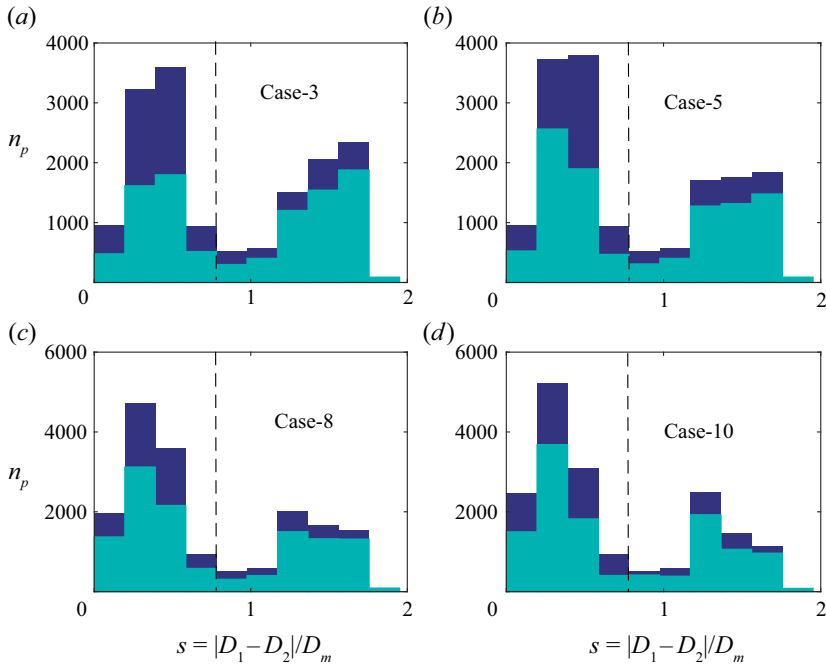
917 A12-12

Figure 9. Droplet pair distribution for a separation distance of $r < 10\eta$ for four different case numbers with $I^* = 14.2\,\%$. Blue and cyan portions of the histograms represent correlated and uncorrelated pairs, respectively.

In figure 9(*a*), we re-plotted the data from figure 6(*b*) for case-3, now with the correlated (non-colliding) and uncorrelated (colliding) pairs within each bin being distinguished by the blue and cyan colours, respectively. While the majority of caustic pairs were colliding, the continuous pairs showed significant fractions for both the colliding and non-colliding pairs. Specifically, of all the continuous and caustic pairs, 50.5 % and 76.2 % contributed to collisions, respectively. Figure 9(*b–d*) shows the same plot as in figure 9(*a*), but for cases 5, 8 and 10. Overall, the total number of continuous (caustic) pairs increased (decreased) with case no., which resulted from a combined effect of increasing ρ_N and decreasing $\bar{D}$. Of all the droplet pairs contributing to collision, the number of uncorrelated continuous pairs seemed to increase with case no., while the number of caustic pairs decreased. It is, however, prudent to normalize these numbers with the total number of observed droplet pairs, which we proceeded to do in figure 10.

The total number of uncorrelated/colliding pairs (continuous and caustic) for a given case no., denoted as $N_{p,uc}$, was estimated by summing up all the cyan regions in the corresponding histogram plots such as those in figure 9. Denoting the total number of droplet pairs by N_p, we estimated the fraction of uncorrelated droplet pairs $N_{p,uc}/N_p$ for all the experiments, and plotted this as a function of $\bar{D}$ (figure 10*a*) and ρ_N (figure 10*b*). We observed a gradual increase in $N_{p,uc}/N_p$ from case 1 to case 7, i.e. as $\bar{D}$ (ρ_N) decreased (increased) from 35 μm (832 cm^{-3}) to 22 μm (1495 cm^{-3}). A sudden increase was then observed in going from case 7 to case 8, which resulted in relatively large values of $N_{p,uc}/N_p$ for cases 8 to 11. Interestingly, the sudden increase occurred at the same ρ_N value as for the overall droplet size growth rate R^* (figure 4*b*).
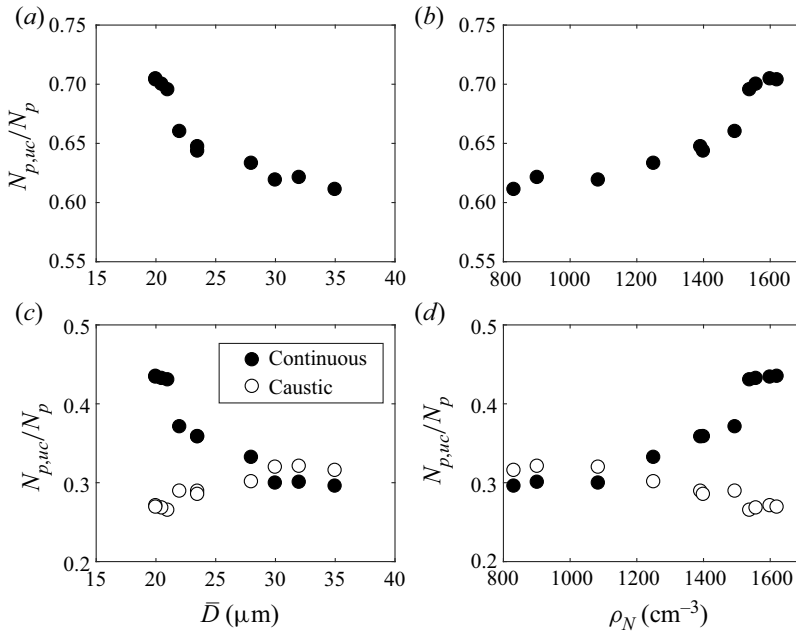
Figure 10. Variations in fraction of uncorrelated ($N_{p,uc}$) droplet pairs with (a) $\bar{D}$ and (b) ρ_N. The relative contribution to uncorrelated pairs from the continuous (filled circles) and caustic (unfilled circles) pairs, plotted as a function of (c) $\bar{D}$ and (d) ρ_N.

In the bottom row of figure 10, the fraction of uncorrelated droplet pairs are further split into contributions from continuous (filled circles) and caustic (unfilled circles) droplet pairs. In contrast to the trends in $N_{p,uc}/N_p$, the contribution from the caustic pairs increased (decreased) with $\bar{D}$ (ρ_N). It is worth noting that an increase in $\bar{D}$ introduced a larger number of inertial droplets, which in turn would increase the number of caustic pairs. However, the uncorrelated continuous pairs captured the trends in $N_{p,uc}/N_p$, which suggested that collision dynamics associated with the continuous pairs plays a critical role in understanding the trends in R^* versus ρ_N. In summary, the introduction of a larger number of smaller droplets seems to increase the overall collision rates, with a further sharp increase beyond a threshold value of ρ_N. As shown in Appendix E, independent measurements from PDI also confirm that progressively smaller droplets contribute more to the overall collision rates as we move from case 1 to case 11.

While the increase in the number of continuous pairs with a decrease (increase) in $\bar{D}$ (ρ_N) is expected, the increase in the fraction of uncorrelated continuous pairs is less straightforward to understand. The mechanism of increased droplet velocity fluctuations as a result of adding a large number of small droplets in a turbulent flow (Sahu, Hardalupas & Taylor 2016) could potentially corroborate our observation of an increase in the fraction of uncorrelated continuous pairs with ρ_N. Towards this objective, we plotted the droplet root mean square (rms) axial velocity based on PDI measurements in the different cases (figure 11a). Indeed, for droplets with sufficiently small Stokes number, i.e. $St < 1$ (the kind that make up continuous pairs), u_{rms} increased with an increase in ρ_N. A similar trend was observed for two other droplet classes, very small droplets ($St < 0.2$) and all droplets ($St < 30$). Interestingly, the positive deviation of u_{rms} for $St < 1$ from u_{rms} in very small droplets ($St < 0.2$) suggested that droplets in continuous pairs encountered
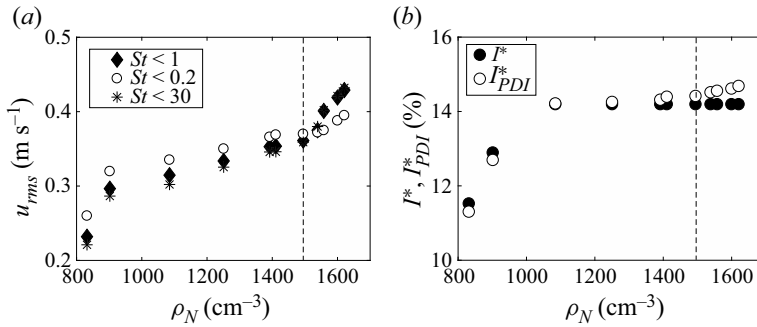
Figure 11. (*a*) Variation of rms of droplet axial velocity fluctuations with ρ_N for three different droplet classes. (*b*) Variation with ρ_N of LDV-based optimum turbulence intensity I^* for maximum droplet size growth. Corresponding PDI-based turbulence intensities, as estimated from the rms velocity of small droplets ($St < 0.2$), are shown using unfilled circles. The dashed vertical line is drawn at the value of ρ_N above which R^* increases rapidly with ρ_N.

larger fluctuations than what is suggested by the flow turbulence. A sudden increase in u_{rms} beyond a threshold ρ_N was also observed, again at the same threshold as for R^*. Overall, the velocity fluctuations increased by a factor of approximately 1.45 in going from $\rho_N = 1085$ to 1621 cm^{-3}, which suggested that an increased mass loading modulates the flow turbulence (Parthasarathy & Faeth 1990). In other words, the turbulence intensity I_{PDI}, as estimated from the rms velocity of sufficiently small droplets ($St < 0.2$), increased with ρ_N though the LDV-based turbulence intensity I measured without the spray was held constant (figure 11*b*). With the increased fluctuations observed for all droplet classes, it is reasonable to expect that the flow turbulence intensity is lower at a large mass loading (Gore & Crowe 1991). This further suggests that $St < 0.2$ may not faithfully represent flow tracers at a large mass loading.

While the overall increase in u_{rms} with ρ_N is consistent with the observations of Gualtieri *et al.* (2013) and Sahu *et al.* (2016), the physical mechanism behind the sudden increase in u_{rms} beyond $\rho_N = 1495$ cm^{-3} remains unclear. One potential mechanism that explains this sudden increase is the enhanced inertial-droplets-induced fluctuations in smaller droplets (Shao, Wu & Yu 2012). Specifically, the presence of an inertial droplet ($St \gg 1$) could alter the flow field around it, which in turn induces enhanced velocity fluctuations in smaller droplets in its vicinity. To quantify this mechanism in our experiments, we used the LDM images to identify close encounters of continuous pairs with inertial droplets.

A schematic representation of the method we employed to identify (and quantify) close encounters of continuous droplet pairs (one such pair denoted by the filled circles) with inertial particles (an inertial particle denoted by unfilled circle) is shown in figure 12(*a*). For each of the identified continuous droplet pairs, we located the relatively faster moving inertial droplet (identified as $d_i > 40$ μm, corresponding to $St = 2.8$; $St < 2.8$ droplets within a distance of 15η from the continuous pairs were observed not to move significantly faster than the continuous pairs) that was closest to the continuous pair when they simultaneously occupied the same axial location. As shown in figure 12(*a*), the occurrence of the continuous pair and the inertial droplet being at the same axial location could occur at a back-tracked trajectory location outside the LDM frame as well. The separation distance between the continuous pair and the inertial droplet of the closest encounter was measured as Δr at the instance when they were at the same axial location (more details of
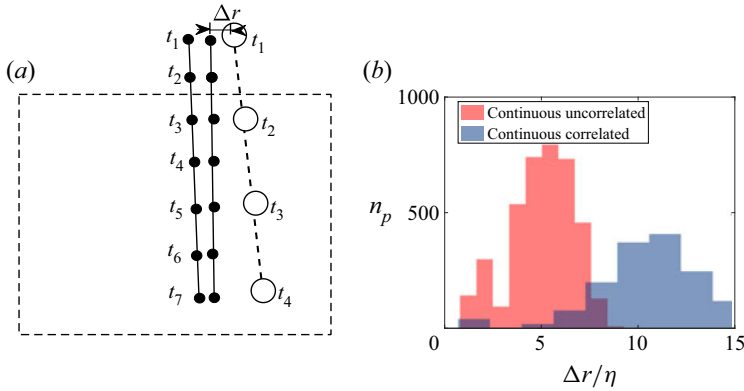
Figure 12. (*a*) Schematic showing how close encounters of a continuous droplet pair (filled circles) with an inertial droplet (unfilled circle) are quantified. (*b*) Statistical distribution of $\Delta r/\eta$ for uncorrelated continuous and correlated continuous droplet pairs from the case-3 experiment ($\rho_N = 1085\ \text{cm}^{-3}$ and $\bar{D} = 30\ \mu\text{m}$).

the method used to estimate Δr is provided in Appendix C). Statistical distributions of Δr for continuous droplet pairs were then plotted to verify if uncorrelated continuous pairs were indeed subject to stronger velocity fluctuations from nearby inertial droplets.

The distributions of $\Delta r/\eta$, where η is the Kolmogorov length scale, for the correlated continuous and uncorrelated continuous pairs, as measured in the case-3 experiment, are shown in figure 12(*b*). The mean values $(\overline{\Delta r/\eta})$ estimated from the distributions were 5.03 and 10.52 for the uncorrelated continuous and correlated continuous pairs, respectively. In other words, figure 12(*b*) shows that uncorrelated continuous pairs experienced noticeably closer encounters with inertial droplets when compared with the correlated continuous pairs. We observed a similar trend for all the other experimental case numbers as well. As discussed in Shao *et al.* (2012), these closer encounters with inertial droplets increase velocity fluctuations in smaller droplets, which in turn could reduce the correlation within continuous droplet pairs. In figure 13, the variation of $\overline{(\Delta r/\eta)}$ with ρ_N, i.e. across the various experiments, for the uncorrelated continuous pairs is shown. For $\rho_N \leq 1495\ \text{cm}^{-3}$, a gentle decrease in $\overline{\Delta r/\eta}$ with ρ_N was observed, which would further increase the velocity fluctuations on top of what is already caused by the increased mass loading. Interestingly, we also observed a sudden rapid decrease in $\overline{\Delta r/\eta}$ at the same value of ρ_N at which the droplet size growth rate also suddenly increased. In fact, for the largest ρ_N value that we investigated, inertial droplets seemed to be present often at distances of the order of the Kolmogorov length scale from continuous droplet pairs. It is worth recalling that the sudden rapid decrease in $\overline{\Delta r/\eta}$ predominantly arose from the increase in ρ_N, as $\bar{D}$ varied insignificantly for $\rho_N \geq 1495\ \text{cm}^{-3}$.

In summary, while the overall increase (with ρ_N) of the fraction of uncorrelated continuous pairs is understood as a result of mass loading and inertial-droplets-induced velocity fluctuations, the sudden increase beyond a threshold ρ_N is attributed entirely to the sudden increase in very close encounters with inertial droplets. One possible mechanism for the sudden increase in close encounters with inertial droplets could be the initiation of a moving out of smaller droplets from the eddies beyond a certain fluctuation level (Ghosh *et al.* 2005), which in turn allows the small droplets to explore highly strained regions in the flow where inertial droplets are often present (Bec *et al.* 2011). It is also noteworthy that the polydispersity decreased with ρ_N in our experiments. At a given ρ_N, an increase in
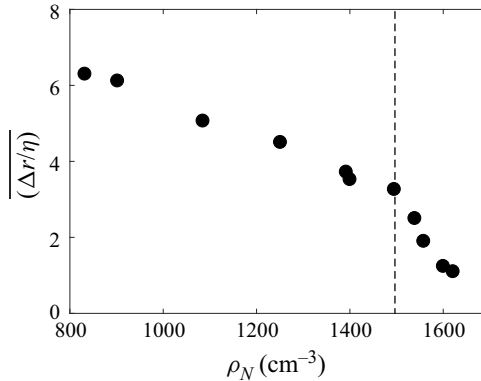
Figure 13. Variation of $\overline{(\Delta r/\eta)}$ (estimated from distributions for uncorrelated continuous droplet pairs such as that shown in figure 12*b*) with ρ_N across all the case numbers. The dashed vertical line is drawn at the value of ρ_N above which R^* increases rapidly with ρ_N.

polydispersity would result in an increase in the number density of inertial droplets, which in turn would strengthen the mechanism of an encounter of inertial droplets by continuous droplet pairs. Holding the polydispersity constant would therefore have resulted in a more dramatic increase of R^* with ρ_N.

4. Conclusions

In this paper, we have presented an experimental study of the effect of droplet number density on droplet size growth rate in strongly polydisperse (droplet diameters in the range of 0–120 µm) droplet fields occurring in a background turbulent air flow (characterized by turbulence intensity I). Experiments were performed for eleven different initial droplet field characteristics, across which the droplet number density ρ_N and the mean droplet size $\bar{D}$ were varied. Specifically, ρ_N was varied from approximately 800 cm^{-3} to approximately 1600 cm^{-3}, while $\bar{D}$ varied from 35 to 20 µm. Based on PDI measurements, we have shown that an optimum air turbulence intensity I^* (approximately 14 %), at which the droplet size growth rate is maximised, exists for each of the eleven initial droplet field characteristics. The occurrence of clustering for $I > I^*$ was found to be the underlying physical mechanism for the existence of an optimum turbulence intensity for all the initial droplet field characteristics. As ρ_N ($\bar{D}$) was increased (decreased), the maximum droplet size growth rate R^* (approximately 180 µm s^{-1}) was observed to not significantly vary up to a threshold ρ_N of approximately 1495 cm^{-3}. For ρ_N larger than the threshold, R^* was observed to rapidly increase with an increase in ρ_N, while $\bar{D}$ was held nearly constant. Specifically, R^* increased from 185 to 274 µm s^{-1} as ρ_N was increased from 1495 to 1621 cm^{-3}, while $\bar{D}$ was held at approximately 21 $\pm$ 0.5 µm.

The rapid increase in R^* above a threshold ρ_N was then understood in terms of droplet pair dynamics, visualized and quantified using LDM. In all our experiments, three kinds of droplet pairs were observed: (i) uncorrelated continuous pairs, which comprised similar-sized small droplets with a temporally changing separation distance between the droplets; (ii) correlated continuous pairs, which comprised similar-sized small droplets with the corresponding separation distance remaining nearly constant with time; and (iii) caustic pairs, which comprised a small and a large droplet whose separation distance changed rapidly with time. Statistical distributions of these three droplet pair categories

were then plotted, with the uncorrelated continuous pairs and caustic pairs contributing to droplet collisions. Interestingly, above the threshold ρ_N at which R^* increases rapidly, the fraction of uncorrelated continuous pairs also rapidly increases with ρ_N. Further analysis of the continuous pairs revealed that close encounters with inertial droplets rapidly increase their velocity fluctuations beyond the threshold ρ_N, which in turn rapidly increases the fraction of uncorrelated continuous pairs. In summary, beyond a threshold droplet number density in a polydisperse droplet field, aided by velocity fluctuations caused by close encounters with inertial droplets, droplet collision rates associated with small droplets can become substantial.

The air turbulence, while being characterized in the current study by LDV in the flow without the droplet field, is modified by the droplet field in our experiments, especially at large ρ_N. Signatures of such turbulence modification are shown in figure 11 based on PDI data for small droplets, and would be worth studying more carefully in future studies. The modified air turbulence characteristics may also modify the values of the droplet Stokes numbers, which we defined using the LDV-based turbulence characteristics. However, our main conclusion that droplet collisions increase sharply owing to increased encounters of small droplet pairs with inertial droplets does not hinge on precise estimates of Stokes numbers associated with various droplet sizes. Moreover, the intention of the current study was to hold the background turbulence characteristics (without the droplet field) constant, and vary only the initial droplet field characteristics. The modification of air flow turbulence characteristics is then a consequence of the initial droplet field characteristics, predominantly the number density in our experiments.

The results reported in this paper have implications for rain formation. Typically, small droplets in a cloud can grow up to a diameter of approximately 30 µm by diffusion of water molecules, and larger droplets ($>$100 µm) grow through coalescence induced by gravitational settling (Pruppacher & Klett 1997). Mechanisms driving droplet growth through the bottleneck diameter range of 30–100 µm (Wang & Grabowski 2009) are not well understood, with air turbulence being one of the primary candidates (Falkovich *et al.* 2002). The extent to which air turbulence may contribute to droplet size growth depends also on droplet characteristics such as number density and polydispersity. For example, previous studies (Devenish *et al.* 2012) on clouds with a very narrow distribution of droplet diameter have reported an impending delay in rain formation because collisions between small similar-sized droplets are less likely. In contrast, in deep cumulus clouds, collisions between similar-sized droplets are found to contribute significantly to the droplet size growth even for diameter ranges where condensation is conventionally thought to be the dominant mechanism (Chen, Yau & Bartello 2018). The underlying mechanisms for enhanced collisions between similar-sized small droplets in the cumulus cloud are not well understood. Our study provides a potential mechanism: beyond a threshold droplet number density, the presence of large droplets in polydisperse droplet fields can rapidly accelerate collision between similar-sized small droplets. This mechanism also offers a potential answer to earlier reports (Langmuir 1948) that large droplets formed by accretion in warm rain or from the melting of ice flakes in cool rain are alone not sufficient to explain the sudden onset of rains; the occurrence of small droplet pairs whose collisions are enhanced by larger droplets is also required.

Several avenues could be pursued in the future as a follow-up to our study. Previous studies have demonstrated that in a monodisperse droplet field, the relative velocity of $St \ll 1$ droplets is solely governed by the separation distance r (Saffman & Turner 1956; Bec *et al.* 2005). In a polydisperse droplet field, however, the mechanism of enhanced velocity fluctuations by close encounters with inertial droplets needs to be taken into account in models for collisions and coalescence. Droplet coalescence resulting

from droplet collisions is often arbitrarily assumed to be 100 % efficient in numerical studies though there are studies that suggest otherwise (Pinsky, Khain & Krugliak 2008; Bordás *et al.* 2013). It would be worthwhile to investigate the effect of turbulence on collision–coalescence efficiency in laboratory experiments. Further, the roles of larger spatial scales (and hence larger Reynolds number for the background airflow than what was possible in our experiments) and the anisotropy of turbulence (Nicolai *et al.* 2014) in the clouds are also to be investigated. It would also be worthwhile to explore the trends observed in this paper in field data obtained under various atmospheric conditions.

Declaration of interests. The authors report no conflict of interest.

Author ORCIDs.
ⓘ Manikandan Mathur https://orcid.org/0000-0002-2133-3889.

Appendix A. Droplet and flow characteristics

In this appendix, we present the definition of various droplet and flow characteristics that we estimated from PDI and LDV measurements.

Droplet characteristics, such as global size distribution $n(d_i)$, mean droplet diameter $\bar{D}$ and Sauter mean diameter SMD, were estimated from the PDI measurements for the individual droplets with a diameter of d_i passing through the PDI probe volume. In every experiment, the initial droplet size distribution was characterized by the global size distribution at $x = 100$ mm, an axial location at which secondary atomization has finished. Specifically, it was estimated as (Tratnig & Brenn 2010)

$$n(d_i) = \frac{1}{\Delta d} \frac{\displaystyle\sum_{j=1}^{j=J} \dot{n}(|y_j|, d_i)|y_j|}{\displaystyle\sum_{j=1}^{J} \sum_{i=1}^{I} \dot{n}(|y_j|, d_i)|y_j|}, \tag{A1}$$

where Δd and $\dot{n}(|y_j|, d_i)$ are the width of the diameter class centred around d_i and the number flux of the corresponding diameter class at a radial location y_j. The corresponding mean droplet diameter $\bar{D}$ and the SMD associated with the initial droplet field are estimated as

$$\bar{D} = \frac{\displaystyle\sum_{i=1}^{B} n(d_i)d_i}{\displaystyle\sum_{i=1}^{B} n(d_i)}, \quad SMD = \frac{\displaystyle\sum_{i=1}^{B} n(d_i)d_i^3}{\displaystyle\sum_{i=1}^{B} n(d_i)d_i^2}. \tag{A2a,b}$$

At subsequent axial locations in the region of interest, i.e. 200 mm $\leq x \leq$ 400 mm, individual droplet sizes from various radial locations are gathered to define the mean
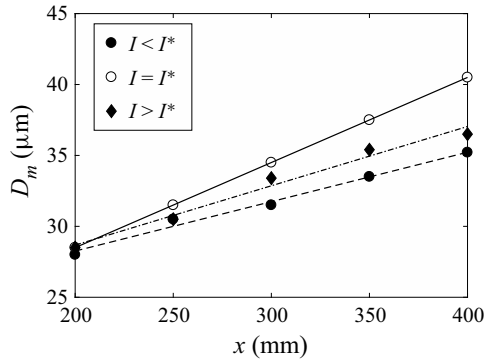
Figure 14. Variation of D_m with axial location x in the case-3 spray nozzle experiments (see table 2) for three different turbulence intensities ($I < I^*$, $I = I^*$ and $I > I^*$).

diameter D_m as

$$D_m = \frac{\displaystyle\sum_{i=1}^{B} N_i d_i}{\displaystyle\sum_{i=1}^{B} N_i}, \quad (A3)$$

where N_i is the number of droplets corresponding to the diameter class centred around d_i and B is the total number of bins. A typical curve of $D_m(x)$ for three different turbulent intensities from the case-3 spray nozzle experiments is shown in figure 14. Compared with the other two turbulent intensities, the slope in $D_m(x)$ was larger at the optimum turbulence intensity of I^*. The droplet size growth rate was estimated from the slope of $D_m(x)$, as described in the beginning of § 3.

LDV measurements were used to characterize the flow turbulence in the absence of the droplet field. The turbulent intensity was estimated as

$$I = \frac{U_{rms}}{U_m}, \quad (A4)$$

where $U_{rms} = \sqrt{(u_{rms}^2 + v_{rms}^2 + w_{rms}^2)/3}$ and $U_m = \sqrt{u_m^2 + v_m^2 + w_m^2}$. Here, u_{rms}, v_{rms} and w_{rms} are the rms of the flow velocity along the x-, y- and z-axes, respectively, measured at a specific location. Corresponding mean velocities are u_m, v_m and w_m. Similar turbulence intensity estimates were also made from PDI measurements, using velocities of droplets whose diameter lay within a specified range. In the PDI estimates, we assumed $w_{rms} = v_{rms}$ and $w_m = v_m$ based on the isotropy of the flow.

In addition to the turbulence intensity, other turbulence characteristics were also estimated from the LDV data. In general, various length scales can be estimated from the power spectral density (PSD) of the flow velocity fluctuations. To account for the non-uniform arrival of olive oil droplets in the LDV probe volume, the sample-and-hold (S+H) method of interpolation (Benedict, Nobach & Tropea 2000) was used to generate time series with uniform sampling, thus making the LDV data suitable for the PSD estimates (Adrian & Yao 1986). From these re-sampled values, the autocorrelation of

917 A12-20

time-series data of velocity fluctuations is computed as

$$R(\tau) = \frac{\langle u'(t)u'(t+\tau) \rangle}{\langle u'(t)^2 \rangle}, \tag{A5}$$

where $\langle \ \rangle$ denotes the ensemble average, $u'(t)$ is the fluctuating velocity component and τ is the time lag. The area under the autocorrelation coefficient until the first zero-crossing is integrated to obtain the integral time scale as (Pope 2000; Mulla *et al.* 2019)

$$\tau_{int} = \int_0^{t_0} R(\tau)\,d\tau, \tag{A6}$$

where t_0 denotes the time of the first zero-crossing of the correlation coefficient. The integral length scale is then calculated as $L = u_m\tau_{int}$, where u_m is the measured mean axial velocity.

The one-dimensional frequency spectra of velocity fluctuations $E(k)$ were obtained from the normalised auto-correlation function $R(\tau)$ by using the Fourier cosine transform (Nobach, Müller & Tropea 1998). To estimate the dissipation rate ϵ, we assumed the energy spectrum $E(k)$ to be described by $E(k) = C_k\epsilon^{2/3}k^{-5/3}$ in the inertial range (Adrian & Yao 1986), where C_K and k are the Kolmogorov constant and wave number, respectively. Assuming isotropic turbulence, the corresponding Kolmogorov length scale η, Taylor microscale λ and Reynolds number based on the Taylor microscale were estimated as (Pope 2000)

$$\eta = (\nu^3/\epsilon)^{1/4}, \quad \lambda = (15\nu/\epsilon)^{1/2}u_{rms}, \quad Re_\lambda = \lambda u_{rms}/\nu, \tag{A7a–c}$$

where u_{rms} is the the root mean square of the velocity fluctuations and ν the kinematic viscosity.

Appendix B. Clustering estimate using pair correlation function (PCF)

To quantify clustering in our experiments, the pair correlation function (PCF) was estimated from the PDI measurements. The temporal pair correlation function is a measure of the deviation of droplet arrival time distribution at a fixed spatial location from the Poisson distribution, and is estimated as (Larsen *et al.* 2005)

$$PCF(t) = \frac{r(t)}{p(t)} - 1. \tag{B1}$$

Here, $r(t)$ is the number of droplet pairs which have their droplet arrivals at the given location separated within a time in the range $[t - dt/2, t + dt/2]$. $p(t)$ is the corresponding number of droplet pairs with a separation time of the same interval if the droplet arrivals follow a Poisson process. In other words, if the droplet arrivals at the given location follow a Poisson process, the corresponding $PCF(t)$ would be uniformly zero, which indicates that there is no clustering in the flow. However, a relatively large value for $PCF(t)$ indicates a stronger preference for the corresponding inter-particle arrival time t; in the presence of clustering, such a preference would be for a small t.

In figure 15, PCF estimates for $I \leq I^*$ and $I > I^*$ from the case-3 and case-9 experiments are shown. In figures 15(a) and 15(c) (corresponding to case-3 and case-9, respectively), $PCF(t)$ for three different values of $I \leq I^*$ were observed to be approximately 0 for all t. A similar trend was found in all the other cases for $I \leq I^*$, which suggested that negligible clustering occurred for $I \leq I^*$ across all the cases. For $I > I^*$ (figures 15(b) and 15(d)), large $PCF(t)$ values were observed at small t, which resulted from small inter-particle arrival times associated with droplet clustering.
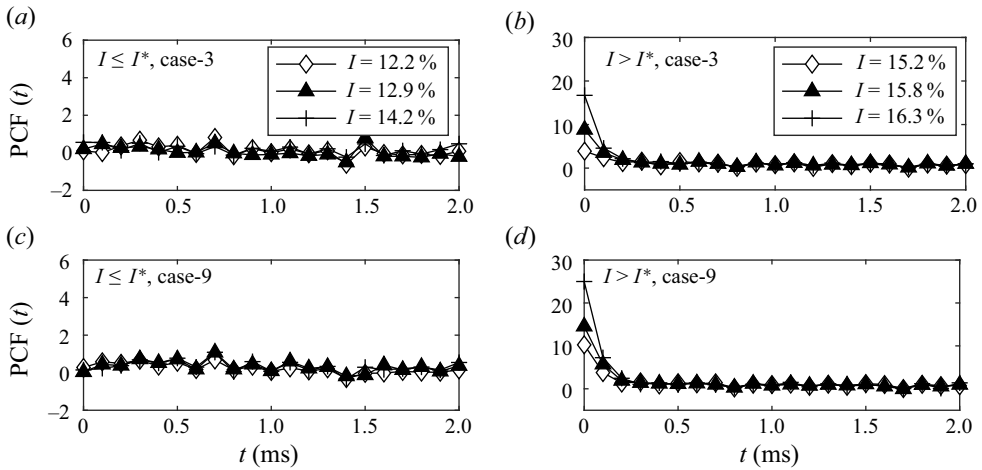
Figure 15. Temporal pair correlation function calculated at $(x, y) = (300, 0)$ mm in the experiments for case 3 (a,b) and case 9 (c,d) for different turbulent intensities. The left and right columns correspond to $I \le I^*$ ($I = 12.2\%$, 12.9% and 14.2%), and $I > I^*$ ($I = 15.2\%$, 15.8% and 16.3%), respectively.

Appendix C. Post-processing of LDM images

In this appendix, we briefly describe how droplet boundaries were extracted from LDM images, which were analysed further to obtain droplet pair characteristics. In figure 5(a), a raw LDM image after background subtraction (for the background, an image captured with the same optical arrangements but without any spray droplets was used) is shown. Droplet edges were detected using the MATLAB image processing toolbox, where an appropriate thresholding was done to detect the maximum number of droplets (figure 5b). Droplet diameters were then estimated based on the method described in Blaisot & Yon (2005). The separation distance r between two droplets was estimated as the distance between their effective centroids, as shown in figure 5(b). To avoid double-counting of droplet pairs during droplet pair identification, we used every 10th frame from the 30 000 frames obtained at 10 kHz. Every frame was, however, used to track the evolution of individual droplet pairs.

For individual droplet tracking, droplet centroids and diameters (Blaisot & Yon 2005) were computed and tabulated for each frame. Between the first two consecutive frames in which a droplet appeared, the initial matching was performed by a search for the nearest downstream droplets within a circular sector, as described in Hassan & Canaan (1991) and Bordás *et al.* (2013). The dominant mean axial velocity in the flow helped to reduce the search area to a small circular sector oriented in the axial direction. If multiple matchings were found for a single droplet, the diameter values were used to find the exact match.

Figure 16 shows representative LDM images with the trajectory (dotted lines) of a continuous pair (shown as tiny circles) and an inertial droplet (shown as big circles). For the current study, the distance Δr was between the continuous droplet pair and the inertial droplet measured at the axial location where the inertial droplet overtook the continuous pair. Although approaching inertial droplets were also able to introduce fluctuations in continuous droplet pairs, significant fluctuations occurred mainly when the continuous droplet pairs were in the wake of inertial droplets. Therefore, when a fast moving inertial droplet overtook a continuous droplet pair, the resulting fluctuations were accounted in terms of the distance Δr when they were at the same axial location (figure 16). Although
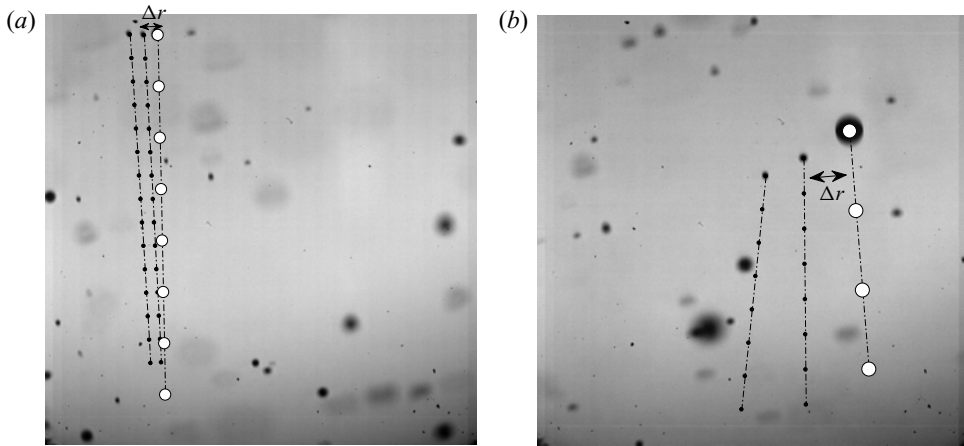
Figure 16. Two representative LDM images showing the measurement of Δr, the distance between a continuous pair and a nearby inertial droplet when they occupy the same axial location. Small circles are continuous pair droplets and the large circle (white filled) corresponds to the inertial droplet.

the closest encounter between the continuous droplet pair and the inertial droplet need not occur when they are at the same axial location, the relatively high axial velocity of the inertial droplet compared with the slow moving continuous droplet pair suggests that Δr was a reasonably good measure of the closest encounter.

Appendix D. Relative velocity of droplet pairs

From the LDM-based droplet trajectories (Appendix C), the droplet pair radial relative velocity γ for each detected droplet pair was estimated as (Dou *et al.* 2018)

$$\gamma(r) = (\boldsymbol{v}_1 - \boldsymbol{v}_2) \cdot \boldsymbol{r}/|r|, \tag{D1}$$

where $\boldsymbol{v}_1$ and $\boldsymbol{v}_2$ are the droplet velocities, and $\boldsymbol{r}$ is the separation vector that goes from droplet 2 to 1. Here, $\gamma(r) < 0$ and $\gamma(r) > 0$ imply that the droplets are moving towards and away from each other, respectively.

In figure 17, the PDF of γ for four different case numbers, considering only those droplet pairs with $r < 10\eta$, are shown. The PDFs for all the cases were symmetric about $\gamma = 0$, with a sharp peak at $\gamma = 0$. This trend in the PDFs of droplet radial relative velocity was qualitatively similar to previously-reported PDFs of particles in turbulent flows (Pan & Padoan 2013; Dou *et al.* 2018). Specifically, Pan & Padoan (2013) showed that the stretched exponential behaviour near the peak corresponds to small *St* particle pairs and the amplification in tails corresponds to caustics. Across all our experiments, the droplet pairs of radial relative velocity in the range $-0.1 < \gamma < 0.1$ m s^{-1} had an average *s* value of $\bar{s} = 0.4$ or lower. In other words, the near-vicinity region of the peak in the PDFs of γ mostly comprised continuous correlated droplet pairs. However, the large γ ($|\gamma| > 1.5$ m s^{-1}) region was dominated by caustic droplet pairs, which resulted in a relatively larger average *s* value of 1.1 or more. The average value of *s* in the intermediate regime of moderate values of γ ($0.1 < |\gamma| < 1.5$ m s^{-1}) was approximately 0.5, which indicated a predominance of continuous uncorrelated droplet pairs.

Beyond the threshold ρ_N above which droplet size growth rapidly increases (case 9 and case 11 in figure 17), both the peak (around $\gamma = 0$) and the tail (large $|\gamma|$) in the PDFs of γ became weaker compared with the cases with a smaller droplet number density (case
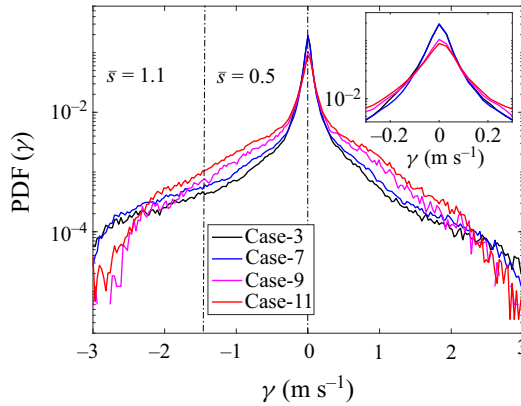
Figure 17. PDFs of radial relative velocity γ estimated using droplet tracking from the LDM images for four different cases. The inset shows the zoomed-in view near the peak of the PDFs. Cases 9 and 11 lay in the regime where a rapid increase in the droplet size growth rate with ρ_N was observed.
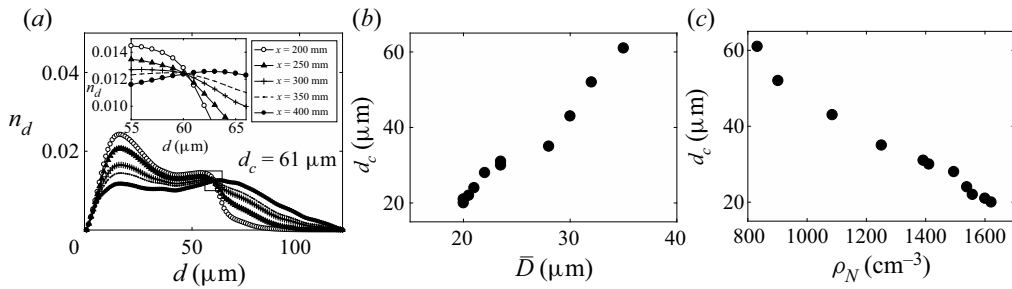

Figure 18. (*a*) Droplet size distribution at different axial locations x for the case-1 experiment. The inset shows the zoomed-in view of the region around the cross-over diameter d_c. Variation of d_c with (*b*) mean droplet size $\bar{D}$ and (*c*) droplet number density ρ_N, as obtained from the eleven different cases.

3 and case 7 in figure 17). Correspondingly, the fraction of continuous uncorrelated pairs (moderate γ in figure 17) increased beyond the threshold ρ_N. These results indicated the increased fraction (and hence the role) of continuous uncorrelated pairs and a decreased fraction of caustic pairs when ρ_N is increased beyond the threshold, and are consistent with the results reported in figure 10.

Appendix E. Cross-over diameter and effect of ρ_N

Based on figure 10, we reported a reduction in caustic pairs with an increase (decrease) in $\rho_N(\bar{D})$, i.e. in going from case 1 to case 11. In this appendix, we verify the same trend from the droplet size distributions estimated using PDI measurements. In figure 18(*a*), the droplet size distributions at different x locations for case 1 at $I = I^*$ are shown. Interestingly, all the distributions nearly intersected within a small range of droplet diameters (inset of figure 18*a*). The median of all these intersections was termed as the cross-over diameter d_c, and was physically interpreted as the maximum droplet diameter that undergoes effective collisions. Detailed analysis of the collision and coalescence rates based on the cross-over diameter is reported in Kumar *et al.* (2019). For each combination of background turbulence intensity and nozzle characteristics, a unique d_c was observed in

917 A12-24

our experiments. Variation of d_c at $I = I^*$ with different $\bar{D}$ and ρ_N is shown in figures 18(b) and 18(c), respectively. With the decrease (increase) in $\bar{D}(\rho_N)$, we observed a decrease in d_c, which suggested the significantly increased collision statistics of smaller droplets than larger droplets. Our earlier observation that the number of caustic pairs reduces with ρ_N, and the increased collision rates of smaller droplets as observed from the decrease in d_c, substantiated the conclusion of increased collisions from uncorrelated continuous pairs at large ρ_N.

REFERENCES

ABRAHAMSON, J. 1975 Collision rates of small particles in a vigorously turbulent fluid. *Chem. Engng Sci.* **30** (11), 1371–1379.

ADRIAN, R.J. & YAO, C.S. 1986 Power spectra of fluid velocities measured by laser doppler velocimetry. *Exp. Fluids* **5** (1), 17–28.

ALISEDA, A., CARTELLIER, A., HAINAUX, F. & LASHERAS, J.C. 2002 Effect of preferential concentration on the settling velocity of heavy particles in homogeneous isotropic turbulence. *J. Fluid Mech.* **468**, 77–105.

BACHALO, W.D. 1997 Measurement techniques for turbulent two-phase flow research. Presented at the *International Symposium on Multiphase Fluid, Non-Newtonian Fluid and Physicochemical Fluid Flows (ISMNP), October 7–9, 1997, Beijing, China.*

BALACHANDAR, S. & EATON, J.K. 2010 Turbulent dispersed multiphase flow. *Annu. Rev. Fluid Mech.* **42**, 111–133.

BEC, J., BIFERALE, L., CENCINI, M., LANOTTE, A.S. & TOSCHI, F. 2010 Intermittency in the velocity distribution of heavy particles in turbulence. *J. Fluid Mech.* **646**, 527–536.

BEC, J., BIFERALE, L., CENCINI, M., LANOTTE, A.S. & TOSCHI, F. 2011 Spatial and velocity statistics of inertial particles in turbulent flows. *J. Phys.: Conf. Ser.* **333**, 012003.

BEC, J., CELANI, A., CENCINI, M. & MUSACCHIO, S. 2005 Clustering and collisions of heavy particles in random smooth flows. *Phys. Fluids* **17** (7), 073301.

BENEDICT, L.H., NOBACH, H. & TROPEA, C. 2000 Estimation of turbulent velocity spectra from laser doppler data. *Meas. Sci. Technol.* **11** (8), 1089–1104.

BLAISOT, J.B. & YON, J. 2005 Droplet size and morphology characterization for dense sprays by image processing: application to the diesel spray. *Exp. Fluids* **39** (6), 977–994.

BORDÁS, R., ROLOFF, C., THÉVENIN, D. & SHAW, R.A. 2013 Experimental determination of droplet collision rates in turbulence. *New J. Phys.* **15** (4), 045010.

BORÉE, J., ISHIMA, T. & FLOUR, I. 2001 The effect of mass loading and inter-particle collisions on the development of the polydispersed two-phase flow downstream of a confined bluff body. *J. Fluid Mech.* **443**, 129–165.

BRACCO, A., CHAVANIS, P.H., PROVENZALE, A. & SPIEGEL, E.A. 1999 Particle aggregation in a turbulent Keplerian flow. *Phys. Fluids* **11** (8), 2280–2287.

CHEN, S., YAU, M.K. & BARTELLO, P. 2018 Turbulence effects of collision efficiency and broadening of droplet size distribution in cumulus clouds. *J. Atmos. Sci.* **75** (1), 203–217.

COLEMAN, S.W. & VASSILICOS, J.C. 2009 A unified sweep-stick mechanism to explain particle clustering in two-and three-dimensional homogeneous, isotropic turbulence. *Phys. Fluids* **21** (11), 113301.

DEVENISH, B.J., *et al.* 2012 Droplet growth in warm turbulent clouds. *Q. J. R. Meteorol. Soc.* **138** (667), 1401–1429.

DOOLEY, P.N. & QUINLAN, N.J. 2009 Effect of eddy length scale on mechanical loading of blood cells in turbulent flow. *Ann. Biomed. Engng* **37** (12), 2449.

DOU, Z., IRELAND, P.J., BRAGG, A.D., LIANG, Z., COLLINS, L.R. & MENG, H. 2018 Particle-pair relative velocity measurement in high-Reynolds-number homogeneous and isotropic turbulence using 4-frame particle tracking velocimetry. *Exp. Fluids* **59** (2), 30.

EATON, J.K. & FESSLER, J.R. 1994 Preferential concentration of particles by turbulence. *Intl J. Multiphase Flow* **20**, 169–209.

FALKOVICH, G., FOUXON, A. & STEPANOV, M.G. 2002 Acceleration of rain initiation by cloud turbulence. *Nature* **419** (6903), 151.

FALKOVICH, G. & PUMIR, A. 2007 Sling effect in collisions of water droplets in turbulent clouds. *J. Atmos. Sci.* **64** (12), 4497–4505.

FREUD, E. & ROSENFELD, D. 2012 Linear relation between convective cloud drop number concentration and depth for rain initiation. *J. Geophys. Res.* **117**, D02207.

GHOSH, S., DAVILA, J., HUNT, J.C.R., SRDIC, A., FERNANDO, H.J.S. & JONAS, P.R. 2005 How turbulence enhances coalescence of settling particles with applications to rain in clouds. *Proc. R. Soc. Lond.* A **461** (2062), 3059–3088.

GOOD, G.H., IRELAND, P.J., BEWLEY, G.P., BODENSCHATZ, E., COLLINS, L.R. & WARHAFT, Z. 2014 Settling regimes of inertial particles in isotropic turbulence. *J. Fluid Mech.* **759**, R3.

GORE, R.A. & CROWE, C.T. 1991 Modulation of turbulence by a dispersed phase. *Trans. ASME J. Fluids Engng* **113** (2), 304–307.

GOTO, S. & VASSILICOS, J.C. 2008 Sweep-stick mechanism of heavy particle clustering in fluid turbulence. *Phys. Rev. Lett.* **100** (5), 054503.

GRABOWSKI, W.W. & WANG, L.-P. 2013 Growth of cloud droplets in a turbulent environment. *Annu. Rev. Fluid Mech.* **45**, 293–324.

GUALTIERI, P., PICANO, F., SARDINA, G. & CASCIOLA, C.M. 2012 Statistics of particle pair relative velocity in the homogeneous shear flow. *Physica* D **241** (3), 245–250.

GUALTIERI, P., PICANO, F., SARDINA, G. & CASCIOLA, C.M. 2013 Clustering and turbulence modulation in particle-laden shear flows. *J. Fluid Mech.* **715**, 134–162.

HASSAN, Y.A. & CANAAN, R.E. 1991 Full-field bubbly flow velocity measurements using a multiframe particle tracking technique. *Exp. Fluids* **12** (1–2), 49–60.

JACOBS, C.N., MERCHANT, W., JENDRASSAK, M., LIMPASUVAN, V., GURKA, R. & HACKETT, E.E. 2016 Flow scales of influence on the settling velocities of particles with varying characteristics. *PloS One* **11** (8), e0159645.

JAMES, M. & RAY, S.S. 2017 Enhanced droplet collision rates and impact velocities in turbulent flows: the effect of poly-dispersity and transient phases. *Sci. Rep.* **7** (1), 12231.

KUMAR, M.S., CHAKRAVARTHY, S.R. & MATHUR, M. 2019 Optimum air turbulence intensity for polydisperse droplet size growth. *Phys. Rev. Fluids* **4** (7), 074607.

LANGMUIR, I. 1948 The production of rain by a chain reaction in cumulus clouds at temperatures above freezing. *J. Meteorol.* **5** (5), 175–192.

LARSEN, M.L., KOSTINSKI, A.B. & TOKAY, A. 2005 Observations and analysis of uncorrelated rain. *J. Atmos. Sci.* **62** (11), 4071–4083.

MAXEY, M.R. 1987 The gravitational settling of aerosol particles in homogeneous turbulence and random flow fields. *J. Fluid Mech.* **174**, 441–465.

MONCHAUX, R., BOURGOIN, M. & CARTELLIER, A. 2010 Preferential concentration of heavy particles: a voronoïanalysis. *Phys. Fluids* **22** (10), 103304.

MONCHAUX, R., BOURGOIN, M. & CARTELLIER, A. 2012 Analyzing preferential concentration and clustering of inertial particles in turbulence. *Intl J. Multiphase Flow* **40**, 1–18.

MULLA, I.A., SAMPATH, R. & CHAKRAVARTHY, S.R. 2019 Interaction of lean premixed flame with active grid generated turbulence. *Heat Mass Transfer* **55** (7), 1887–1899.

NICOLAI, C., JACOB, B., GUALTIERI, P. & PIVA, R. 2014 Inertial particles in homogeneous shear turbulence: experiments and direct numerical simulation. *Flow Turbul. Combust.* **92** (1–2), 65–82.

NOBACH, H., MÜLLER, E. & TROPEA, C. 1998 Efficient estimation of power spectral density from laser doppler anemometer data. *Exp. Fluids* **24** (5–6), 499–509.

PAN, L. & PADOAN, P. 2013 Turbulence-induced relative velocity of dust particles. I. Identical particles. *Astrophys. J.* **776** (1), 12.

PARTHASARATHY, R.N. & FAETH, G.M. 1990 Turbulence modulation in homogeneous dilute particle-laden flows. *J. Fluid Mech.* **220**, 485–514.

PINSKY, M., KHAIN, A. & KRUGLIAK, H. 2008 Collisions of cloud droplets in a turbulent flow. Part 5. Application of detailed tables of turbulent collision rate enhancement to simulation of droplet spectra evolution. *J. Atmos. Sci.* **65** (2), 357–374.

POPE, S.B. 2000 *Turbulent Flows.* Cambridge University Press.

PRUPPACHER, R.H. & KLETT, J.D. 1997 *Microphysics of Clouds and Precipitation, vol 18. Atmospheric and Oceanographic Sciences Library*. Kluwer Academic Publishers.

QIU, H.-H. & SOMMERFELD, M. 1992 A reliable method for determining the measurement volume size and particle mass fluxes using phase-doppler anemometry. *Exp. Fluids* **13** (6), 393–404.

READE, W.C. & COLLINS, L.R. 2000 Effect of preferential concentration on turbulent collision rates. *Phys. Fluids* **12** (10), 2530–2540.

REVEILLON, J. & VERVISCH, L. 2005 Analysis of weakly turbulent dilute-spray flames and spray combustion regimes. *J. Fluid Mech.* **537**, 317–347.

SAFFMAN, P.G.F. & TURNER, J.S. 1956 On the collision of drops in turbulent clouds. *J. Fluid Mech.* **1** (1), 16–30.

SAHU, S., HARDALUPAS, Y. & TAYLOR, A.M.K.P. 2016 Droplet–turbulence interaction in a confined polydispersed spray: effect of turbulence on droplet dispersion. *J. Fluid Mech.* **794**, 267–309.

SHAO, X., WU, T. & YU, Z. 2012 Fully resolved numerical simulation of particle-laden turbulent flow in a horizontal channel at a low Reynolds number. *J. Fluid Mech.* **693**, 319–344.

SQUIRES, K.D. & EATON, J.K. 1991 Preferential concentration of particles by turbulence. *Phys. Fluids* A **3** (5), 1169–1178.

SUMBEKOVA, S., CARTELLIER, A., ALISEDA, A. & BOURGOIN, M. 2017 Preferential concentration of inertial sub-Kolmogorov particles: the roles of mass loading of particles, stokes numbers, and Reynolds numbers. *Phys. Rev. Fluids* **2** (2), 024302.

SUNDARAM, S. & COLLINS, L.R. 1997 Collision statistics in an isotropic particle-laden turbulent suspension. Part 1. Direct numerical simulations. *J. Fluid Mech.* **335**, 75–109.

TRATNIG, A. & BRENN, G. 2010 Drop size spectra in sprays from pressure-swirl atomizers. *Intl J. Multiphase Flow* **36** (5), 349–363.

VAILLANCOURT, P.A. & YAU, M.K. 2000 Review of particle–turbulence interactions and consequences for cloud physics. *Bull. Am. Meteorol. Soc.* **81** (2), 285–298.

VOSSKUHLE, M., PUMIR, A., LÉVÊQUE, E. & WILKINSON, M. 2014 Prevalence of the sling effect for enhancing collision rates in turbulent suspensions. *J. Fluid Mech.* **749**, 841–852.

WANG, L.-P. & GRABOWSKI, W.W. 2009 The role of air turbulence in warm rain initiation. *Atmos. Sci. Lett.* **10** (1), 1–8.

WANG, L.-P., XUE, Y., AYALA, O. & GRABOWSKI, W.W. 2006 Effects of stochastic coalescence and air turbulence on the size distribution of cloud droplets. *Atmos. Res.* **82** (1), 416–432.

WILKINSON, M., MEHLIG, B. & BEZUGLYY, V. 2006 Caustic activation of rain showers. *Phys. Rev. Lett.* **97** (4), 048501.